Nanoscale Advances

PAPER

View Article Online
View Journal | View Issue

Check for updates

Cite this: *Nanoscale Adv.*, 2022, **4**, 4418

Synergies in antimicrobial treatment by a levofloxacin-loaded halloysite and gold nanoparticles with a conjugation to a cell-penetrating peptide†

Reza Taheri-Ledari, *[a] Mohammad Reza Ahghari,[a] Fatemeh Ansari,[a] Mohadeseh Forouzandeh-Malati,[a] Seyedeh Shadi Mirmohammadi,[a] Simindokht Zarei-Shokat,[a] Sorour Ramezanpour, [b] Wenjie Zhang,[c] Ye Tian*[d] and Ali Maleki *[a]

Received 2nd July 2022
Accepted 13th September 2022

DOI: 10.1039/d2na00431c

rsc.li/nanoscale-advances

Herein, a novel designed antimicrobial therapeutic drug delivery system is presented, in which halloysite nanotubes (HNTs) encapsulate a determined dosage of levofloxacin (lvx). Moreover, gold nanoparticles (AuNPs) have been embedded into the structure for plasmonic heating under irradiation of the green LED light (7 W, 526 nm). It was revealed that the plasmonic heating of the AuNPs leads to a controlled trend in the lvx release process. Also, a synergistic effect on the antimicrobial activity of the prepared therapeutic system has been observed through photothermal heating of the structure. To enhance the cell adhesion, a cell-penetrating peptide sequence (CPP) is conjugated to the surfaces. This CPP has led to quick co-localization of the prepared nano-cargo (denoted as lvx@HNT/Au–CPP) with the bacterial living cells and further attachment (confirmed by confocal microscopy). Concisely, the structure of the designed nano-cargo has been investigated by various methods, and the *in vitro* cellular experiments (zone of inhibition and colony-counting) have disclosed that the antimicrobial activity of the lvx is significantly enhanced through incorporation into the HNT/Au–CPP delivery system (drug content: 16 wt%), in comparison with the individual lvx with the same dosage. Hence, it can be stated that the bacterial resistance against antibiotics and the toxic effects of the chemical medications are reduced through the application of the presented strategy.

1. Overview

In the field of advanced drug delivery, utilization of natural-based micro and nanomaterials for encapsulation of the target drug has increased due to the brilliant factors as follows: showing more structural stability than the artificial species such as metal–organic frameworks,[1–3] having high levels of biodegradability and compatibility,[4,5] capability to combine with organic and inorganic materials,[6,7] sensitivity to external stimuli such as heat and pH.[8,9] Moreover, the surface of this type of material can be chemically modified and functionalized for further conjugations.[10–12] In the broad spectrum of natural-based materials, clay-based nanostructures such as montmorillonite, bentonite, perlite, and other silicate materials have shown substantial potential to be exploited in different applications.[13–15] Among all clay-based species, halloysite nanotubes (HNTs), one of the most well-known clay materials, are particularly preferred for drug delivery due to their unique morphology.[16–18] According to the literature, the rod-shaped morphology (also needles and tubes) of drug carriers significantly affects the cell adhesion, internalization, and uptake processes.[19,20] As a result, more of the administered nanocargo is taken by the living cells during a short contact time, resulting in more efficacy. In addition, HNTs follow a layer-by-layer pattern for the encapsulation of drug molecules, which subsequently results in the sustained release behavior.[21] So far, there have been several reports in which HNTs were employed for

---

[a] *Catalysts and Organic Synthesis Research Laboratory, Department of Chemistry, Iran University of Science and Technology, Tehran 16846-13114, Iran. E-mail: Rezataheri13661206@gmail.com; R_Taheri94@alumni.iust.ac.ir; maleki@iust.ac.ir; Fax: +98-21-73021584; Tel: +98-21-73228313*

[b] *Department of Chemistry, K. N. Toosi University of Technology, P.O. Box 15875-4416, Tehran, Iran*

[c] *Department of Nuclear Medicine, West China Hospital, Sichuan University, No. 37, Guoxue Alley, Chengdu 610041, Sichuan Province, P.R. China*

[d] *State Key Laboratory of Oral Diseases & National Clinical Research Center for Oral Diseases, Department of Orthodontics, West China Hospital of Stomatology, Sichuan University, No.14, 3rd section of South Renmin Road, Chengdu 610041, P.R. China. E-mail: tianye@scu.edu.cn*

† Electronic supplementary information (ESI) available: The ESI file includes the information of the used materials and equipment, calculations related to the drug release screening, and the photos of the colony-count disks. See **https://doi.org/10.1039/d2na00431c**

drug delivery purposes. For instance, Khodabakhshi and Baghersad used a magnetized system based on HNTs for the delivery of vancomycin to bacterial strains.[22] It was revealed that great co-localization was obtained for the HNTs and targeted bacterial cells, which resulted in an acceptable cell death ratio. Also, we previously experimented with heat-sensitivity of the HNTs that was exploited for the controlled release of taxotere (a cytotoxic agent) in ovarian cancer cells.[23] In fact, the effects of plasmonic heating of gold nanoparticles (incorporated into the carrier's structure) on the drug release process was studied, and it was disclosed that a temperature-triggered release can be executed by the HNTs as the drug carrier.

Gold nanoparticles (AuNPs) are a substantial class of pure metallic nanomaterials that have been known for their surface plasmon resonance (SPR) effect.[24] Concisely, AuNPs can be converted into hot spots upon exposure to a specific wavelength of the electromagnetic spectrum, depending on their sizes.[25–27] This exclusive optical property has been used in different medical scopes, such as photodynamic therapy of cancers.[28] The surface of AuNPs can be functionalized with organic and inorganic compounds that include thiol (–SH) groups in their structures.[29,30] It has been revealed that AuNPs can create tight bonds with thiol groups under specific SPR conditions. *Via* this method, so many therapeutic systems have been designed in which a conjugation between the AuNPs and the sulfur-containing biological ingredients (such as antibodies) is formed.[31,32] In addition to the controlled release in the heat-sensitive drug delivery systems (described above), the plasmonic heating of AuNPs provides a great synergy in cell killing purposes because the living cells are seriously damaged at higher temperatures than 38–40 °C.[21,33,34] As an example for photothermal cell death, Zharov *et al.* reported selective laser killing of bacteria with light-absorbing AuNPs, in which the strong laser-induced SPR effect of clustered gold nanoparticles was the main cause of bacterial damage.[35] Recently, rod-shaped AuNPs were used as photothermal agents for noninvasive photothermal therapy against Gram-negative bacteria by Yougbaré *et al.*[36] Hence, it would be worth designing a drug delivery system containing both AuNPs and antibiotic medication and screening their potential synergies by photothermal cell killing and controlled drug release potencies.

In addition to all of the mentioned merits for the introduced drug delivery systems (based on HNTs and AuNPs), overcoming the bacterial resistance through encapsulation of the target drug into the tubes is another brilliant achievement.[37,38] In fact, since the HNTs include a rolled-plate architecture, the target drug can be led into the interior spaces and also between the rolled walls through a layer-by-layer pattern.[39,40] According to the literature, the bacterial cells are able to make resistance against administered antibiotics over time.[41] In this case, the administrated antibiotic will be deactivated, and its main function will be partially lost.[42] The secreted enzymes by the bacteria are responsible for the created resistance.[43–45] Therefore, layer-by-layer encapsulation of antibiotic drug molecules into the carrier system can be a substantial strategy for disconnecting the drug molecules from targeted bacterial cells and subsequent safety of the subjected drug. This particular advantage makes HNTs a suitable vehicle for drug delivery purposes.

As discussed in the first paragraph of this section, the tubular morphology of the halloysite material is highly preferred by the living cells at the internalization and uptake stages. In fact, this trait is considered as a positive physiological feature that significantly affects the total therapeutic properties of the medicinal cargo. To enhance this feature, the surface of HNTs can be modified by the chemical structures and further functionalized with active biological ingredients such as antibodies,[23] aptamers,[46] folic acid,[47] and peptides.[48] Actually, it has been revealed that the presence of these active components on the surfaces can effectively enhance the cell attachment and further internalization of the cargo into the cells.[49,50] As one of the well-known species of these biologically active ingredients, cell-penetrating peptides (CPPs) have been widely utilized for the enhancement of the cellular uptake.[51,52] CPPs are short-length peptide sequences that include a guanidine functional group in their chemical structures and therefore are able to create effective electrostatic interactions with the negative-charge components that exist in the cell membrane.[52,53] This physicochemical feature can provide a fantastic synergy with the tubular shape of the halloysite material, resulting in highly facilitated internalization of the therapeutic cargo into the target cells. In this study, we chose a guanidine-rich CPP (heptapeptide) sequence to enhance the effectiveness of our designed drug delivery system.

Based on all of the information given above, herein, we present a newly designed drug delivery system constructed with HNTs and incorporated AuNPs and suggest it for clinical utilization in anti-infection treatments. In this way, the AuNPs have been synthesized and incorporated into the pores of the neat HNTs, which were modified by a mercaptosilane compound. Then, levofloxacin (lvx), as a bactericidal quinolone antibiotic drug, has been loaded into the HNTs and well wrapped with a freeze dryer. Finally, the surface of the prepared therapeutic cargo has been functionalized with a CPP sequence including glycine (Gly), alanine (Ala), phenylalanine (Phe), proline (Pro), histidine (His), and arginine (Arg), through the thioester bond conjugation. After full characterization of the structure of the prepared nano-cargo (denoted as lvx@HNT/Au–CPP), the bactericidal potency of the prepared nano-cargo has been precisely investigated in comparison with the controls. Concisely, the great potential of the lvx@HNT/Au–CPP therapeutic nano-cargo (with only 16 wt% of lvx content) in bacterial cell killing has been confirmed by the zone of inhibition (ZOI) and disk counter experiments on both Gram-negative and positive cell lines. In this account, the main concepts of advanced drug delivery, such as cell adhesion, co-localization (as the main stage of cellular uptake), the controlled drug release process, and photothermal therapy (through the SPR effect of the AuNPs), have been precisely studied for the presented antimicrobial nano-cargo.

2. Experimental section

2.1. Materials & equipment

All chemicals and instruments that have been used in this project are listed in Tables 1 and 2.

Table 1 The name and purity of the used chemical materials in the current work

Chemical agent	Brand and purity
Halloysite nanotubes	Sigma-Aldrich, kaolin clay
Levofloxacin ($C_{18}H_{20}FN_3O_4\cdot\frac{1}{2}H_2O$)	Temad Co., Iran
(3-Mercaptopropyl)trimethoxysilane (MPTMS)	Sigma-Aldrich, ≥97.0%
Solvents	Sigma-Aldrich
Protected amino acids	AChem Block Co.
2-Chlorotrityl chloride (CTC)	Sigma-Aldrich, 97.0%
N,*N*-Dimethylformamide (DMF)	Sigma-Aldrich, 99.8%
Dichloromethane (DCM)	Sigma-Aldrich, ≥99.0%
N,*N*-Diisopropylethylamine (DIPEA)	Sigma-Aldrich, ≥99.0%
Triethylsilane (TES)	Sigma-Aldrich, ≥99.0%
Trifluoroacetic acid (TFA)	Sigma-Aldrich, ≥99.0%
Piperidine	Sigma-Aldrich, 99.0%
$HAuCl_4$	Sigma-Aldrich, ≥99.0%
Tetrachloroauric(III) acid trihydrate	Sigma-Aldrich, Supelco, 99%
$NaBH_4$	Sigma-Aldrich, 96.0%
HPLC-grade water	Merck
Synthetic ethanol	Merck, 99%
Synthetic methanol	Merck, 99%
Crystal violet	Merck, ≥90.0%
Lugol's solution	Merck
Paper filter	Whatman (grade 602h, particle retention < 2 μm)
Bacterial cell lines	*E. coli* (ATCC 9637) and *S. aureus* (ATCC 12600)
Agar for cell cultivation	Alfa Aesar H26724.36
Crystal violet	Merck, ≥90.0%

2.2. Preparation methods

2.2.1. Preparation of neat HNTs.

The purchased HNTs (5.0 g, Cas No. 1332-58-7) were grinded *via* ball-milling. The milling conditions were as follows: two-bowl ball-milling (Amin Asia Fanavar Pars Co., IRAN), two grinding bowls horizontally positioned on a rotating supporting disc, sample mass 10 g, zirconia balls with 0.1 mm diameter, ball-to-powder ratio 20, for 2 h, and a rotation speed of 200 rpm. The ground powder was used for sonication to remove the zirconia balls from the

Table 2 The name and model of the used equipment in the current work

Instrument	Brand and model
FT-IR spectroscopy	Shimadzu FT-IR-8400S
EDX spectroscopy	VEGA-TESCAN-XMU
TGA analysis	Bahr-STA 504
DLS analysis	Horiba (SZ-100)
Solid state UV-vis spectroscopy	Shimadzu-UV-2550/220v
XRD	DRON-8 X-ray diffractometer
FESEM	Zeiss Sigma
TEM	Zeiss-EM10C-100 KV
LC-MS	Agilent 6410 Triple Quadrupole, Agilent 1200 series Santa Clara, CA, USA
UV-vis spectroscopy	Beckman DU640
Confocal microscopy	Zeiss LMS 700
Green LED light	SABA (7 W)
Shaker	VWR 5000
Incubator	Sh, Noor Sanat Ferdos
Ultrasonic cleaning bath	Steelco US 80
Autoclave (for sterilization)	Reyhan Teb, 2KW-220v
Freeze dryer	Lyoguard
Vacuum pump	Heidolph Persia LQ1
Ball-mill	Amin Asia Fanavar Pars Co. (Iran)
Thermometer	Fluke (572-2 infrared)
Ultrasound probe	Hielscher (UP100H)
Centrifuge	Beckman Coulter GmbH
Vacuum oven	IQS Directory
Oven	Genlab Ltd
Vortex mixer	OHAUS Europe GmbH

product completely. Totally, fifteen balls were placed in each bowl that were horizontally installed on the equipment. The milling process was performed with 10 min intervals after every 20 min of activity.[54] Then, ground HNTs (4.0 g) were rinsed with a mixture of ethanol and deionized water (1 : 1 v/v) three times *via* centrifugation (4K RCF, 15 min) and re-dispersion by using an ultrasound bath (50 KHz, 100 W L^{-1}), and dried in an oven at 60 °C for a day. Afterward, calcination was carried out on the sample in a furnace at 650 °C for 2 h.[55] Next, acid treatment was done through the dispersion of the calcined HNTs in hydrochloric acid (HCl, 1 M) *via* ultrasonication and then stirring under reflux conditions and a N_2 atmosphere for a day.[56] After cooling down to room temperature, the obtained neat HNTs were washed with acetone three times *via* centrifugation and redispersion using the ultrasound bath.

2.2.2. Surface-modification of HNTs by mercaptosilane. In a round-bottom three necked flask (100 mL), neat HNTs (0.7 g) were dispersed in ethanol (15 mL) *via* ultrasonication for 15 min at room temperature. Then, a solution of 3-mercaptopropyltrimethoxy silane (MPTMS, 12 mL, 20% v/v, in toluene) was prepared and added into the flask drop-by-drop during the stirring at room temperature. After completion of the addition, the content of the flask was stirred under reflux conditions (100 °C) for a day under a N_2 atmosphere. Finally, the obtained mercaptopropylsilane-modified HNTs (MPS-HNTs) were collected *via* centrifugation (4K RCF, 15 min), well washed with ethanol five times *via* centrifugation and redispersion using the ultrasound bath, and dried in an oven at 60 °C.[57]

2.2.3. Preparation of AuNPs. In a glass vial (25 mL), pure water (15.8 mL) and a solution of tetrachloroauric acid salt (0.18 mL, 5.0 mM, in pure water) were well mixed *via* magnetic stirring. Then, a solution of sodium borohydride ($NaBH_4$, 0.4 mL, 1.0 mM, in pure water) was prepared and freshly added into the vial. The emergence of the red color in the solution occurred through the reduction of the gold ions to the pure metallic nanoparticles. Ultimately, a solution of trisodium citrate (0.18 mL, 5.0 mM, in pure water) was added into the vial for stabilization of the formed AuNPs.[21,58,59]

2.2.4. Incorporation of lvx and AuNPs in MPS-HNTs. Initially, for desalination of the as-prepared colloidal AuNPs, the particles were collected through centrifugation (17K CRF, 15 min) and washed several times with ultrapure water. Then, in a glass tube (13 by 100 mm, with a threaded cap), MPS-HNTs (0.3 g) were placed and dispersed in a solution of lvx (3.0 mL, 0.5 M, in deionized water) through ultrasonication for 3 min in an ice bath. At this stage, two drops of ethanol were added into the tube for better dispersion of the MPS-HNTs. In the next stage, AuNPs (3.0 mL of the colloidal dispersion of 0.15 mM by gold) were added into the tube, and the content was shaken for 12 h at room temperature. Finally, the obtained lvx@HNT/Au particles were collected by centrifugation (10K RCF, 15 min), washed three times with deionized water, then redispersed in deionized water (10 mL), and dried by using a freeze dryer.[21,22]

2.2.5. Synthesis of the CPP sequence. Solid-phase peptide synthesis techniques were employed for the synthesis of the CPP sequence.[60] In this regard, 2-chlorotritylchloride (CTC) resin was used as a solid phase, and dimethylformamide (DMF) and dichloromethane (DCM) were used as the dominant solvents. In a glass vessel equipped with a phenolic threaded cap, a sintered glass filter, and a valve at the end, CTC (1.0 g, 0.8 loading capacity) was rinsed several times with DMF and DCM, and then a solution of Fmoc-Gly-OH (1.0 mmol) in DMF (5.0 mL) and diisopropylethylamine (DIEA, 16.0 mmol) was added into the vessel, and the content was shaken for 2 h at room temperature. Next, the CTC seeds were rinsed again with DMF (3 × 10 mL) and then with a solution of methanol (1.5 mL), DMF (12.7 mL), and DIEA (0.7 mL) three successive times. After each stage of the process, the CTC was rinsed with DMF (3 × 10 mL). For the removal of the Fmoc protecting group, the CTC was washed with a solution of piperidine (25% v/v, in DMF) (2 × 12.5 mL, 20 min), and then the Kaiser test was carried out to ensure that the removal of the Fmoc group has been successfully performed.[61] After obtaining a positive result from the test, a solution of Fmoc-Ala-OH (2.0 mmol) and TBTU (2.0 mmol) in DMF (5.0 mL) and DIEA (3.5 mmol) was prepared and added into the vessel. Then, the content was shaken for 2 h at room temperature (TBTU stands for 2-1*H*-benzotriazole-1-yl-1,1,3,3-tetramethylaminium tetrafluoroborate). In the same way, the Fmoc-removal and coupling processes were carried out until the final amino acid was attached, and a hexapeptide sequence was prepared. For the separation of the sequence from CTC and final deprotection, a cocktail containing trifluoroacetic acid (TFA, 20 mL), deionized water (0.5 mL), methanol (0.5 mL), and triethylsilane (TES, 0.8 mL) was prepared in a separate round-bottom flask (100 mL), and the CTC was transferred into the flask and gently stirred in an ice bath for 1 h and then an additional hour at room temperature. The red-color CTC seeds were separated from the mixture through filtration with a sintered glass filter, and the remaining solution was concentrated with a rotary evaporator. Ultimately, cold diethyl ether was dropwise added to the solution while the content was gently stirred in the ice bath. The resulting white sediment was collected *via* filtration, dried in a vacuum oven, and sent for purification by RP-HPLC and identification by LC-MS analysis (Fig. S1, in the ESI section†).

2.2.6. Preparation of the lvx@HNT/Au–CPP nano-cargo. In a glass test tube (100 mm, with a threaded cap), lvx@HNT/Au particles (0.2 g) were dispersed in a mixture of pure water (4.0 mL) and ethanol (2.0 mL) using an ultrasonic ice bath. Then, DIEA (0.2 mL) was added into the tube, and the content was shaken at room temperature. In a separate flask, a solution of the as-synthesized CPP (2.0 mL, 10 mM, in ethanol) was prepared and dropwise added into the tube during orbital shaking in an ice bath (in a beaker). After completion of the addition, the tube was insulated with glass wool and foil, and the shaking was continued for additional 2 h at room temperature. Finally, the obtained lvx@HNT/Au–CPP particles were separated *via* centrifugation (4K RCF, 10 min), washed with pure water, redispersed in pure water, and dried with a freeze-dryer.

2.3. Drug release experiments

First, a calibration curve was obtained for the neat lvx. In this regard, a stock solution of lvx with a concentration of 0.25 mg mL^{-1} was prepared in ethanol; then five solutions were obtained *via* dilution of the stock solution with concentrations of 0.005, 0.010, 0.015, 0.020, and 0.025 mg mL^{-1} in PBS (0.1 M, pH = 6.8) at 37 ± 1.0 °C. Paper filtration (Whatman, grade 1) was used for the removal of particulate matter from the solutions. Then, four samples of lvx@HNT/Au–CPP particles (10.0 mg) were added into round-bottom flasks (25.0 mL) containing 10.0 mL of buffer media as follows: PBS pH = 6.8 and 8.0, and acetate buffer (AcB), 0.1 M, pH = 4.6, at 37 ± 1.0 °C. For plasmonic heating, the localized surface plasmon resonance (LSPR) effect of the AuNPs was induced by a LED source (green light, 7.0 W, 526 nm). For the baseline, four samples of HNT/Au–CPP (10.0 mg) were prepared and experimented under the same conditions. All samples were stirred for 2 h, and after completion of the process, the particles were separated *via* centrifugation (4K, 10 min) and paper filtration. The remaining clear solutions were diluted with related buffer media (1 to 100 mL) and studied on a UV-vis spectrophotometer at a wavelength of 295 nm.[21,62,63]

2.4. Cellular experiments

2.4.1. Primary preparations. To evaluate the antibacterial activity of the lvx@HNT/Au–CPP nano-cargo, the particles were well dispersed in Dulbecco's Modified Eagle Medium (DMEM) and tested against the bacterial strains: *E. coli* (ATCC 9637) and *S. aureus* (ATCC 12600), provided by Pasteur Institute of Iran – Department of Cell Bank. For the particle dispersion, an ultrasonic cleaning bath (50 KHz, 100 W L^{-1}) was used. Each sample was ultrasonicated for three minutes before the subjection to the cells. Cell cultivation was performed on Mueller–Hinton Agar gel (Alfa Aesar H26724.36) in Petri dishes *via* incubation at 37 °C and 95% humidity. All the experiments were performed in a shaking incubator at 37 °C and 180 rpm (Sh, Noor Sanat Ferdos). All glassware was sterilized at 120 °C for 15 minutes using an autoclave (Reyhan Teb, 2KW-220v). To apply LSPR conditions, a green LED light (7 W, 526 nm) was used.

2.4.2. Cell cultivation. Two bacterial strains (*S. aureus* and *E. coli*) were grown on Mueller–Hinton Agar gel in Petri dishes. First, the bacteria cells were prepared in the physiological serum with a concentration of 1.0–1.5 × 10^{8} CFU mL^{-1}. For this aim, the opacity of the solutions was compared with a standard solution of barium chloride 0.5% in sulfuric acid 0.36 N (0.5 McFarland).[64] Then, the prepared cells were poured onto the agar gel surfaces using cotton swabs. Finally, the Petri dishes were put into the incubator and kept for 24 h at 37 ± 1.0 °C and a humidity of 95%.

2.4.3. Evaluation of the zones of inhibition. The dishes containing Mueller–Hinton agar gel were smoothly swept with cell-impregnated swabs. Then, the samples with the same concentration (5.0 mg mL^{-1}) were precisely put on the agar gel, focusing on a well-determined point. For this purpose, the resolvable samples (such as the sole lvx) were dissolved in the buffer medium (PBS, 0.1 M, pH = 6.8), and a disk was impregnated with the solution and carefully put on the gel. The solid particles were dispersed in an ultrasonic cleaning bath (3 min, 30 °C). After the subjection of the samples to the cultivated cells, the Petri dishes were put into the incubator (37 °C, 35% humidity) for 24 h, and the formed zones around the samples were diametrically evaluated. This experiment was repeated three times ($n = 3$) for each sample, and the errors were measured considering the standard deviation (STDEV) values.

2.4.4. Colony counting experiment. For this experiment, a linear cell culture pattern was followed in which inoculation loops were sterilized on the flame, and a thin layer of the desired bacteria colony was transferred onto the agar gel. Afterward, the loop was sterilized again, and the colony was dispersed on the clean areas of the gel. Next, an L-shaped glass rod was sterilized and used for pouring a drop of the sample around the disk (next to the wall). Then, the plate was put into the incubator (37 °C, 95% humidity) for 48 h. After this time, the number of visible colonies was carefully counted and reported. This experiment was repeated three times ($n = 3$) for each sample, and the errors were measured considering the standard deviation (STDEV) values.

3. Results & discussion

3.1. Preparation of the lvx@HNT/Au–CPP nano-cargo

In order to provide more uniform HNTs, ball-milling (with zirconia bowl and balls) was used to break down the longer tubes into smaller ones.[65] To remove the unwanted materials from the interior spaces and to make a neat structure of the ground HNTs, calcination[66] and acid-treatment processes[67] were applied, respectively. Afterward, surface-modification of the neat HNTs by a mercaptosilane compound was considered to create free thiol sites on the surfaces for further formation of thioester bonds with the CPP sequence. Since there are numerous hydroxyl groups on the surface of the HNTs, the mercaptopropylsilane (MPS) attachment is performed through a nucleophilic substitution reaction between the oxygen and silicon atoms.[68] Then, the AuNPs were prepared and incorporated into the pores of the MPS-modified HNTs. At this stage, the prepared AuNPs were dispersed in a solution of lvx and subjected to the MPS-HNTs. The incorporation of both AuNPs and lvx in the porous structure of the HNTs (denoted as lvx@HNT/Au) was fixed *via* physical contraction of the rolled walls with a freeze dryer.[21] A CPP sequence including glycine (Gly), alanine (Ala), phenylalanine (Phe), proline (Pro), histidine (His), and arginine (Arg) was synthesized in the solid phase, according to our previous report.[51] This CPP sequence includes a guanidine functional group at the end of its structure, leading to better cell adhesion and subsequent internalization through electrostatic interactions with the negative-charge ingredient in the cell membrane.[53] As the active chemical site in the structure of the designed CPP, the carboxylic acid group could participate in the formation of thioester bonds with the MPS-HNTs. This conjugation is immediately dissociated under the acidic conditions of the intracellular environment after the uptake process.[69,70] Fig. 1 schematically represents the preparation route of the lvx@HNT/Au–CPP nano-cargo over the successive stages.

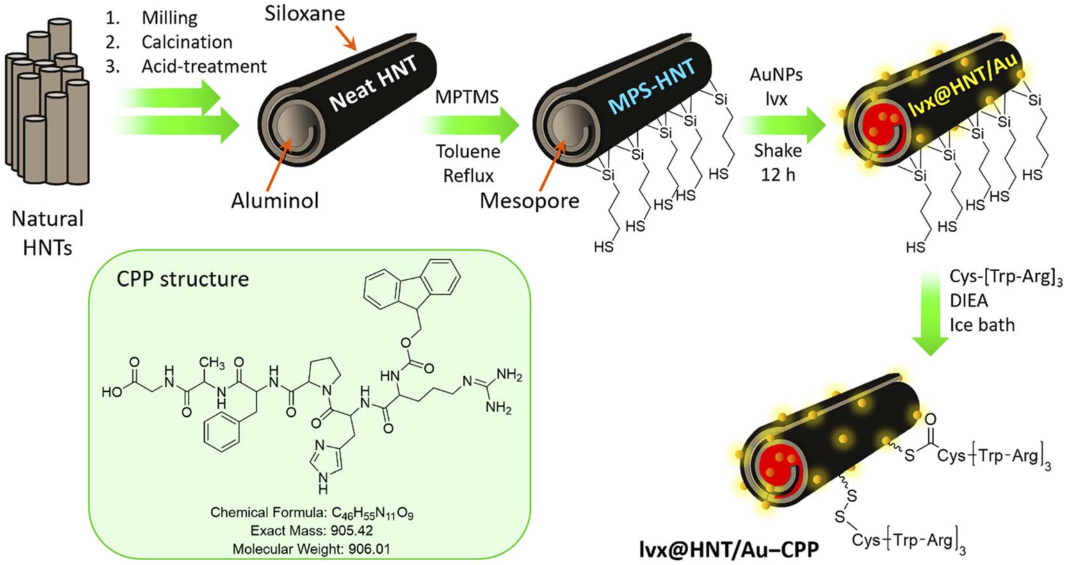

Fig. 1 Schematic presentation of the successive stages in the preparation route of the lvx@HNT/Au–CPP nano-cargo.

3.2. Characterization of the lvx@HNT/Au–CPP nano-cargo

Fourier-transform infrared (FTIR) spectroscopy was used to investigate the functional groups coming from different layers. As is seen in Fig. 2, four spectra related to the neat HNTs (spectrum a), activated HNTs (spectrum b), MPS-HNT (spectrum c), and lvx@HNT/Au–CPP (spectrum d) have been compared to each other. In spectrum (a), a broad peak has appeared in the range of 3000–3600 cm^{-1} coming from the hydroxyl groups of alumina and silica networks of HNTs. Also, a sharp peak related to the bending vibrations of the Si–O–Si band has appeared at *ca.* 1050 cm^{-1} (for all samples).[71] Next to the mentioned peak, relatively small peaks appearing at *ca.* 630 and 840 cm^{-1} are attributed to SiO–H and Si–OH, respectively.[72] In spectrum (b), conversion of the broad peak (at *ca.* 3600 cm^{-1}) to a double keen peak corroborates successful activation of the HNTs, especially the interior layers (alumina).[73] Again, after surface-modifying of the tubes by MPTMS, the separated peaks of AlO–H have been converted to a broad peak, confirming the good coating of the surfaces (spectrum c). As is observed, the intensity of the peak that appeared at *ca.* 2930 cm^{-1} (related to the stretching vibrations of C–H sp^3), increased after surface coating by MPS.[74] This increase originates from the C–H bonds (hybridation sp^3) in the structure of MPS. In spectrum (d) that is related to the lvx@HNT/Au–CPP nano-cargo, it is clearly observed that the intensity of the broad peak of O–H bonds (at 3000–3600 cm^{-1}) has increased, while the peak intensity of Si–O–Si bands (at *ca.* 1050 cm^{-1}) has reduced.[75] This observation well verifies that surface coating by the CPP peptide chain and lvx drug has successfully occurred. In fact, since the CPP peptide sequence and the lvx drug are rich sources of the

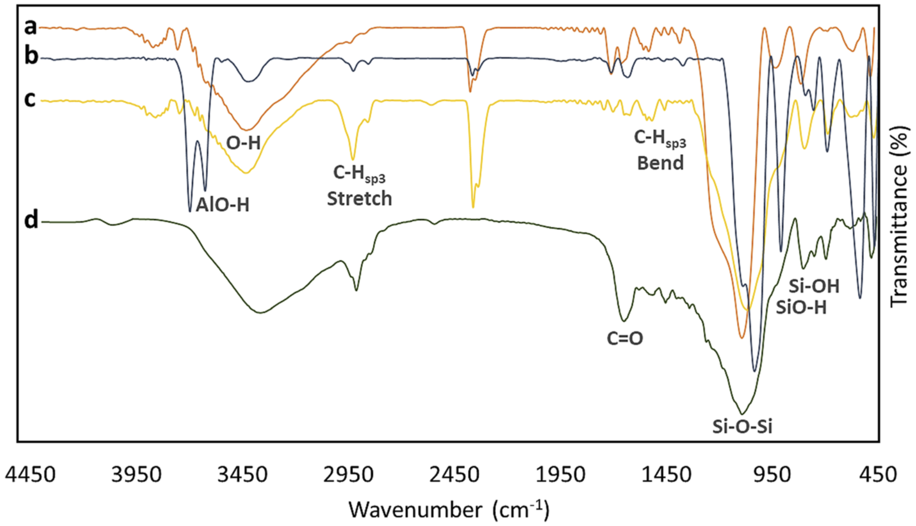

Fig. 2 FTIR spectra of the neat HNTs (a), activated HNTs (b), MPS-HNT (c), and lvx@HNT/Au–CPP (d).

hydroxyl groups, the intensity of the broad peak has increased through the incorporation of them into the structure. In contrast, since the surfaces and the pores of the silica network are coated with the CPP and lvx, the peak intensity of the Si–O–Si band is reduced. Also, a new peak has emerged at 1670 cm^{-1} that is ascribed to the C═O bonds, which is only present in the structure of the CPP sequence and lvx drug.

As another efficient method for investigation of the new layers in the structure, energy-dispersive X-ray (EDX) spectroscopy was performed on the samples, and both quantitative and qualitative results were collected. As presented in Fig. 3, appearance of the peak for the sulfur atom in spectrum (b) (related to MPS-HNT) with a weight percentage of 4.93% confirms surface coating by MPS, as there is no vestige of this atom in spectrum (a) (related to the neat HNTs). In spectrum (c) that is related to lvx@HNT/Au–CPP, the presence of fluorine and gold atoms with weight percentages of 0.29 and 0.4%, respectively, well corroborates successful incorporation of lvx and AuNPs in the structure. For more confirmation, energy-mapping images of the prepared lvx@HNT/Au–CPP nano-cargo are provided as well. As is seen in the d series, the presence of important elements such as silicon (yellow), aluminum (pink), carbon (red), sulfur (orange), and gold (blue) has been proven by the appeared spots in the images.

To investigate the size, morphology and composition state of the particles, field-emission scanning-electron microscopy (FESEM) and transmission-electron microscopy (TEM) were used. As illustrated in Fig. 4a–c, the tubular shape of the halloysite nanoparticles is clearly identified in the FESEM images. As shown in panel (a), the natural HNTs are in an aggregated form before performing the ball-milling process, while dispersion of the particles with a narrower size distribution has been obtained after the grinding process *via* milling (panel b). Also, the brilliant tiny spots among the tubes corroborate the presence of the AuNPs. For better detection, TEM imaging was performed on a dispersed sample of the lvx@HNT/Au–CPP nano-cargo (panel c). As is seen in the TEM image, the dark spots distributed onto the tube represent the AuNPs, which confirms the good composition of the AuNPs with the HNTs. In order to obtain better information of the particle size distribution for the sample of the lvx@HNT/Au–CPP nano-cargo in the colloidal state, intensity-based dynamic-light scattering (DLS) analysis was carried out as well. As presented in Fig. 4d, the natural HNTs have shown a wide peak with an average size of *ca.* 2.8 micrometers, whereas both the PDI and average size decreased for the lvx@HNT/Au–CPP nano-cargo. As is observed in the curves, two values of the mean particle size have been obtained for the lvx@HNT/Au–CPP nano-cargo (blue curve), *ca.* 250 nm and 800 nm. It can be observed that the average size of the particles has decreased to *ca.* 250 nm after the ball-milling process (as confirmed by FESEM imaging), and the second peak (at *ca.* 800 nm) represents the aggregation state of the particles.[76,77]

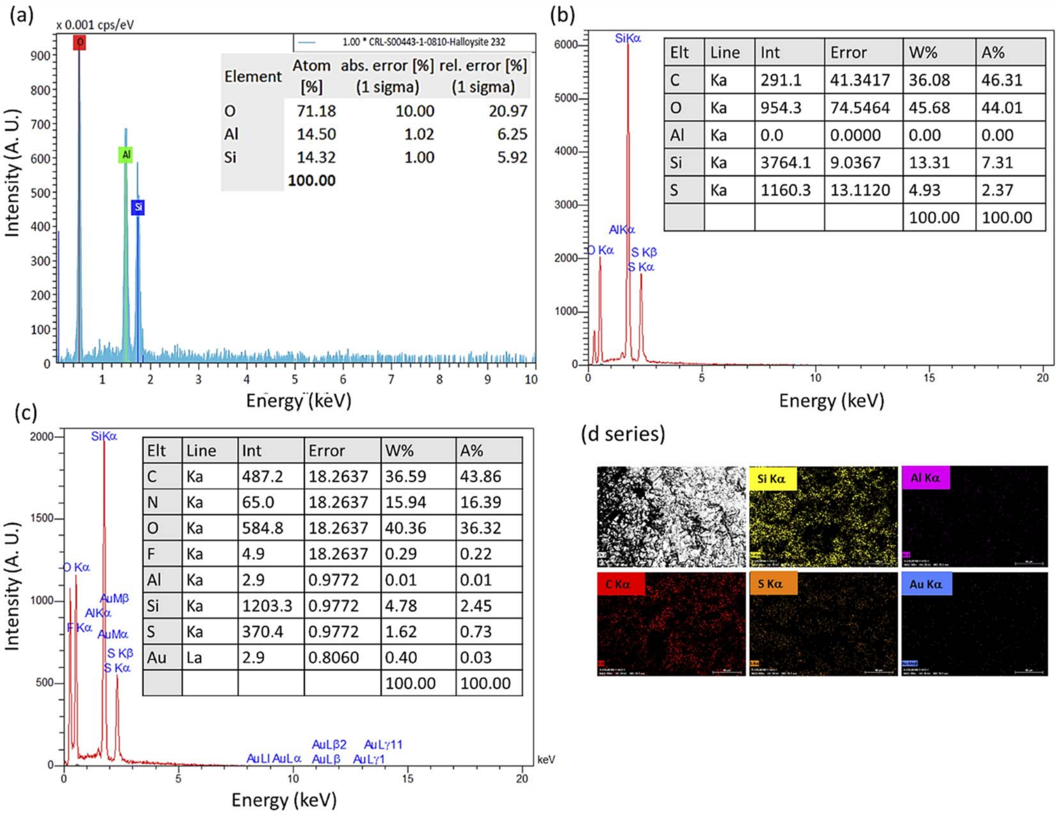

(a)

Element	Atom [%]	abs. error [%] (1 sigma)	rel. error [%] (1 sigma)
O	71.18	10.00	20.97
Al	14.50	1.02	6.25
Si	14.32	1.00	5.92
	100.00		

(b)

Elt	Line	Int	Error	W%	A%
C	Ka	291.1	41.3417	36.08	46.31
O	Ka	954.3	74.5464	45.68	44.01
Al	Ka	0.0	0.0000	0.00	0.00
Si	Ka	3764.1	9.0367	13.31	7.31
S	Ka	1160.3	13.1120	4.93	2.37
				100.00	100.00

(c)

Elt	Line	Int	Error	W%	A%
C	Ka	487.2	18.2637	36.59	43.86
N	Ka	65.0	18.2637	15.94	16.39
O	Ka	584.8	18.2637	40.36	36.32
F	Ka	4.9	18.2637	0.29	0.22
Al	Ka	2.9	0.9772	0.01	0.01
Si	Ka	1203.3	0.9772	4.78	2.45
S	Ka	370.4	0.9772	1.62	0.73
Au	La	2.9	0.8060	0.40	0.03
				100.00	100.00

Fig. 3 EDX spectra of the neat HNTs (a), MPS-HNT (b), and lvx@HNT/Au–CPP (c), and energy-mapping images of the prepared lvx@HNT/Au–CPP nano-cargo (d series).

Thermal decomposition of the samples gives some information about their structures and architectures. Hence, thermogravimetric analysis (TGA) was performed on the samples of the natural HNTs and lvx@HNT/Au–CPP nano-cargo, and the obtained results were compared together. As presented in Fig. 5a, a simple and smooth curve has been obtained for the natural HNTs (red curve), where no significant decrease in the weight is observed within the heating process. In the mentioned curve, as expected, thermal degradation has started from Rel. Mass = 137%, which means that silica and alumina networks have acted as a molecular sieve and highly adsorbed the moisture in air *via* heating up to *ca.* 50 °C.[78] Then, the adsorbed moisture is removed by heating up to around 120 °C. Afterward, the entrapped water molecules inside the underlying layers of the rolled tubes have been gradually removed by increasing the temperature; therefore, a fairly steady trend has been obtained for the natural HNTs. In contrast, no significant water adsorption has occurred for the lvx@HNT/Au–CPP nano-cargo (blue curve), as there has been only a 2.0% increase in the total mass by heating up to *ca.* 50 °C. Therefore, it can be deduced that since the surface of the HNTs has been coated with the MPS and CPP layers, there was no significant vacancy for the moisture in air to be adsorbed. Moreover, it should be noted that the hydrophilicity of the surfaces is reduced through surface coating with the propyl groups present in the structure of the MPS.[79] Hence, less moisture can be adsorbed by the surfaces. As is seen in the curve, a shoulder has appeared in the thermal range of 300–390 °C, which is attributed to the removal of the incorporated lvx and entrapped water molecules into the underlying layers of the HNTs. At this stage, *ca.* 17% of the total weight has been lost. In the next stage, *ca.* 23% of the mass was reduced in the thermal range of 390–700 °C, which is ascribed to the removal of the organic layers such as the CPP peptide sequence and MPS and also degradation of the hydroxyl groups *via* a dehydration process.[22,51] Afterwards, the main structure of the HNTs is most likely degraded.

Ultraviolet-visible diffuse reflectance spectroscopy (UV-DRS) was also performed on the solid samples to study the optical properties of the surfaces. *Via* this method, differences between the structures are in part identified through comparisons. As demonstrated in Fig. 5b, UV-light absorbance activity of the MPS-HNT sample (gray curve) has been enhanced after the incorporation of the additional components into the structure. As is observed, the UV-absorbance activity of the MPS-HNTs at a wavelength of *ca.* 230 nm was reduced after the addition of the AuNPs (red curve). Furthermore, the absorbance value was increased in the range of 270–410 nm. Based on this observation, it can be concluded that the combination of the AuNPs

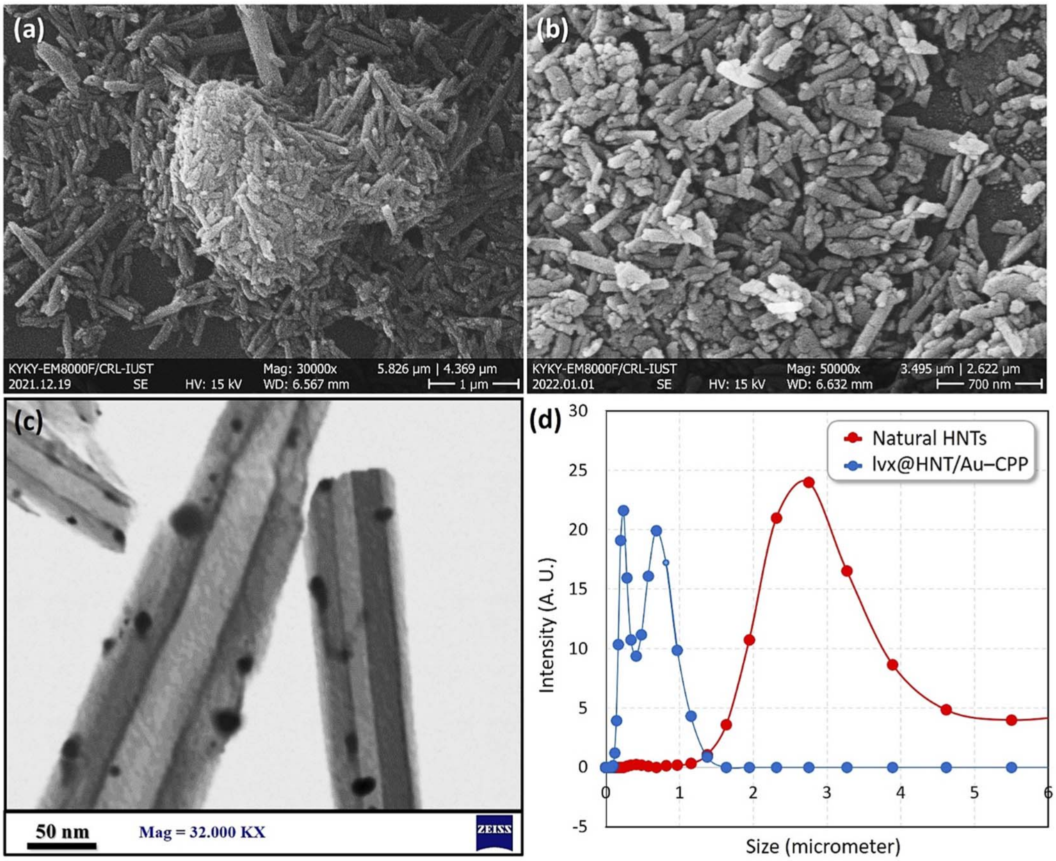

Fig. 4 FESEM images of the neat HNTs (a) and lvx@HNT/Au–CPP nano-cargo (b), the TEM image of the prepared lvx@HNT/Au–CPP nano-cargo (c) [the contrast of the TEM image is 20% enhanced for better illustration of the AuNPs], and intensity-based DLS curves of the natural HNTs and the lvx@HNT/Au–CPP nano-cargo (d).

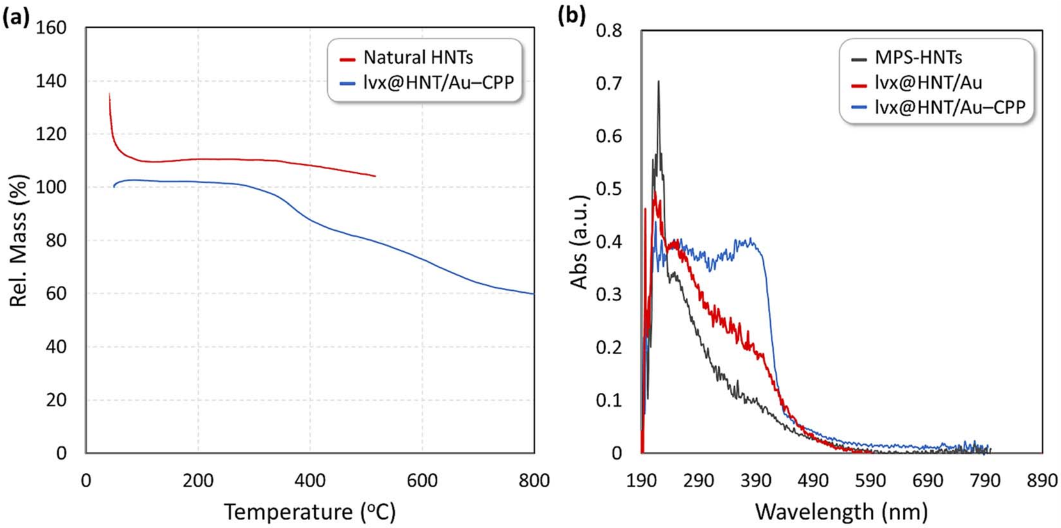

Fig. 5 (a) TGA curves of the natural HNTs (red) and lvx@HNT/Au–CPP nano-cargo (blue), and (b) UV-DRS curves of the natural HNTs (gray), lvx@HNT/Au (red), and lvx@HNT/Au–CPP nano-cargo (blue).

significantly enhances the optical activity of the prepared nano-cargo, which makes it appropriate for photothermal therapy.[80] In the next stage, the CPP peptide sequence and lvx have been incorporated into the structure, and as is observed, the absorbance activity was increased (blue curve). It is clearly seen that the absorbance activity has particularly increased in the range of 300–450 nm. This increase in the UV-absorbance activity can be attributed to the active functional groups in the chemical structure of the CPP chain and lvx.

The X-ray diffraction (XRD) pattern of the prepared lvx@HNT/Au–CPP nano-cargo was provided and compared with the pattern of the natural HNTs and the reference pattern of the AuNPs (JCPDS: 04-0784).[81,82] As exhibited in Fig. 6, the silica and alumina networks of the natural HNTs (red curve) resulted in the broad peaks in the range of $2\theta = 13$–$48°$. There are specifically three indicative broad peaks that represent the amorphous structure of the silica and alumina networks.[83] A part of this broadness is clearly seen in the pattern of lvx@HNT/Au–CPP (orange curve) in the range of $2\theta = 20$–$30°$ as well. From a comparison with the reference pattern of the AuNPs (with icosahedral morphology), three indicative peaks that appeared at $2\theta = 17.0°$, $22.5°$, and $28.1°$ (marked by a star) can be ascribed to three peaks in the pattern of the AuNPs (marked by a star in the blue curve) by considering a shift to the lower angles. According to the literature, several factors can affect the patterns and induce shifting in the location of the XRD peaks.[84,85] There is also another peak in the pattern of lvx@HNT/Au–CPP that has appeared at $2\theta = 12.2°$. This peak can be attributed to the new phase formed on the surface of HNTs through MPS-coating.

3.3. Antimicrobial properties

The antimicrobial properties of the prepared lvx@HNT/Au–CPP nano-cargo were investigated under the typical and LSPR conditions (LSPR stands for localized surface plasmon resonance). For the LSPR conditions, a LED light (7.0 W, green) has been used. Generally, it was intended to induce two benefits into the prepared lvx@HNT/Au–CPP nano-cargo *via* LSPR heating: (1) controlled release of lvx through LSPR heating and physical expansion of the rolled walls,[21] and (2) photothermal killing of the bacterial living cells.[86] In fact, the potential synergies in the antimicrobial activity of the prepared lvx@HNT/Au–CPP nano-cargo are investigated under LSPR conditions. In this way, the content of the loaded lvx inside the tubes and the release behavior in different environments were evaluated according to an approved procedure. Then, the ZOI and colony counting experiments were performed on two

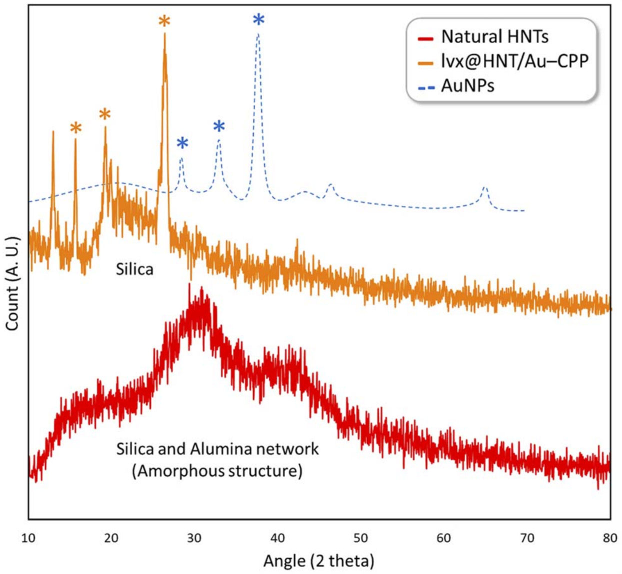

Fig. 6 High-angle XRD patterns of the natural HNTs (red), AuNPs (blue), and lvx@HNT/Au–CPP nano-cargo (orange).

bacterial cell lines: *S. aureus* (Gram-positive) and *E. coli* (Gram-negative). In this regard, the comparisons have been made in the presence of the neat lvx, colloidal sample of AuNPs, the neat CPP, and lvx@HNT/Au as the controls.

3.3.1. Drug release and content screening. A simple method was considered for the estimation of the loaded amount of lvx into the tubes and further release under different conditions.[52,87] Accordingly, the UV-vis absorbance activities of the resultant solutions were studied at a wavelength of 295 nm (related to lvx).[88] To simplify the experiment, other factors that may partially affect the result, such as dimensions of the HNTs, the solubility of the lvx in the buffer media, and diffusivity of the lvx molecules, have not been considered in this study. In the first stage, a calibration curve was drawn for the standard (STD) solutions of lvx in five different concentrations; 5, 10, 15, 20 and 25 ppm. The exact procedure for STD preparation is given in the experimental section of this paper. From the calibration curve, a line equation was obtained and considered in drug release and content calculations (Fig. 7a). Then, four samples of lvx@HNT/Au–CPP particles were added into the buffer-containing flasks (10 mg per 10 mL). Buffer phosphate (PBS) with pH = 6.8 and 8.0 and acetate buffer (AcB) with pH = 4.6 at 37 °C were used for the *in vitro* screening. All samples were stirred for two hours, and after completion of the process, the particles were separated *via* centrifugation and paper filtration. The remaining clear solutions were diluted with the related buffer media (1 to 100 mL) and studied by using a UV-vis spectrophotometer at a wavelength of 295 nm. For the baseline, HNT/Au–CPP particles were stirred under the specified conditions and separated after completion of the process. Next, the remaining supernatant was diluted exactly in the same way as for the lvx@HNT/Au–CPP samples. The obtained UV-vis spectra after a 60 minute process have been illustrated in Fig. 7b. As expected, the maximum release was obtained under the LSPR conditions in the acidic environment. According to the literature, the rolled walls of the HNTs are responsive to localized heating and the acidic environment, and as a result, higher amounts of the loaded drug can be released under these conditions.[21,89] In fact, a physical expansion occurs *via* dissociation of the hydrogen-bond network present between the rolled walls of the HNTs, and the encapsulated drug is conveniently released. For the release-profile study, 0.5 mL of the solutions were withdrawn and added to 49.5 mL of the related buffer solution in the time range of 5–60 minutes (5, 10, 15, 20, 30, 40, and 60 minutes). Then, the removed 0.5 mL was immediately replaced by 0.5 mL of the related buffer solution (37 °C). As presented in Fig. 7c, a pattern similar to the extended release is observed for the release at pH = 6.8. In fact, the loaded drug in the HNTs is sequentially released over the 60 minutes under these conditions. Most likely, since a layer-by-layer strategy is followed by the rolled tubes for encapsulation of the lvx,[22,90] a sequential release has been observed in neutral pH. In the alkaline environment, a controlled release pattern is observed through which the majority of the encapsulated lvx was released over the first 20 minutes. Afterward, the remaining lvx was gradually released over time. A similar pattern is seen for the acidic pH (pH = 4.6), but the difference is that higher values of the loaded lvx have been released during 40 minutes. As referred before this, this may be due to better dissociation of the hydrogen-bond network between the rolled walls under acidic conditions. From a comparison between the curves related to the acidic environment (pH = 4.6 and pH = 4.6 under LSPR conditions), it is found that the complete release of lvx is executed *via* synergies between the acidic conditions and LSPR-heating of the AuNPs. As is observed, a pattern of the controlled release has been obtained in the acidic pH and under irradiation of the green LED light. It is clearly seen that the major release occurred over 15 minutes of irradiation of the LED light. In fact, the release process is immediately triggered upon exposure of the particles to the LED light. According to the literature, plasmonic heating of the AuNPs (incorporated into the HNTs) leads to the rolled wall expansion, and the whole structure is opened.[21,22] As a result, the majority of the encapsulated lvx in the pores and between the layers is immediately released with high control. For the plasmonic heating, the localized surface plasmon resonance (LSPR) effect of the AuNPs was induced by a LED source (green light, 7.0 W, 526 nm) (Fig. 7d). Table 3 briefly presents the calculated amounts of the released lvx under different conditions. If we assume that a complete drug release (100%) occurs at pH = 4.6 and under LSPR conditions, the drug content of the lvx@HNT/Au–CPP nano-cargo is estimated to be *ca.* 16 wt%. Eqn (1) has been considered for the calculation of the released lvx.[91]

$$X = \frac{Y - 0.1227}{0.2941} \times 100 \tag{1}$$

where "X" is the concentration of the released lvx (in ppm) before dilution of the samples, and "Y" is the UV-vis absorbance value (in A.U.) studied after dilution of the samples (1 to 100 mL). The whole equation has been obtained from the linear range of the concentration and absorbance at the calibration curve (Fig. 7a). The detailed calculations have been given in the ESI section†.

3.3.2. Antimicrobial studies. To evaluate the antimicrobial properties of the presented lvx@HNT/Au–CPP nano-cargo, the growth rates of two bacterial strains (*S. aureus* and *E. coli*) were evaluated in the presence of the controls *via* the zone of inhibition (ZOI) test.[92,93] In this way, equal dosages of the lvx@HNT/Au–CPP, lvx@HNT/Au, AuNPs, CPP, and individual lvx were comparatively experimented. Since some of the samples were not dissolved in water, the powder portions were subjected to the cells. In this way, 2.0 mg of all samples were put onto the agar gels that were well swept with the living cells. Then, the disks were incubated at 37 °C and a humidity of 95% for 24 hours. For the LSPR conditions, the disks were exposed to the LED light (7 W, green) for two hours every six hours. As illustrated in Fig. 8a and d, the plates containing lvx@HNT/Au–CPP, lvx@HNT/Au, and individual AuNPs were initially exposed to the LED light before incubation. Then, they were put into the incubator at 37 °C, and the formed zones were diametrically evaluated after completion of the process. As demonstrated in Fig. 8b and e, the largest zones on both cell strains belong to the lvx@HNT/Au–CPP particles. As is observed, the growth inhibition zones with diameters of (3.53 ± 0.13) cm and (4.72 ±

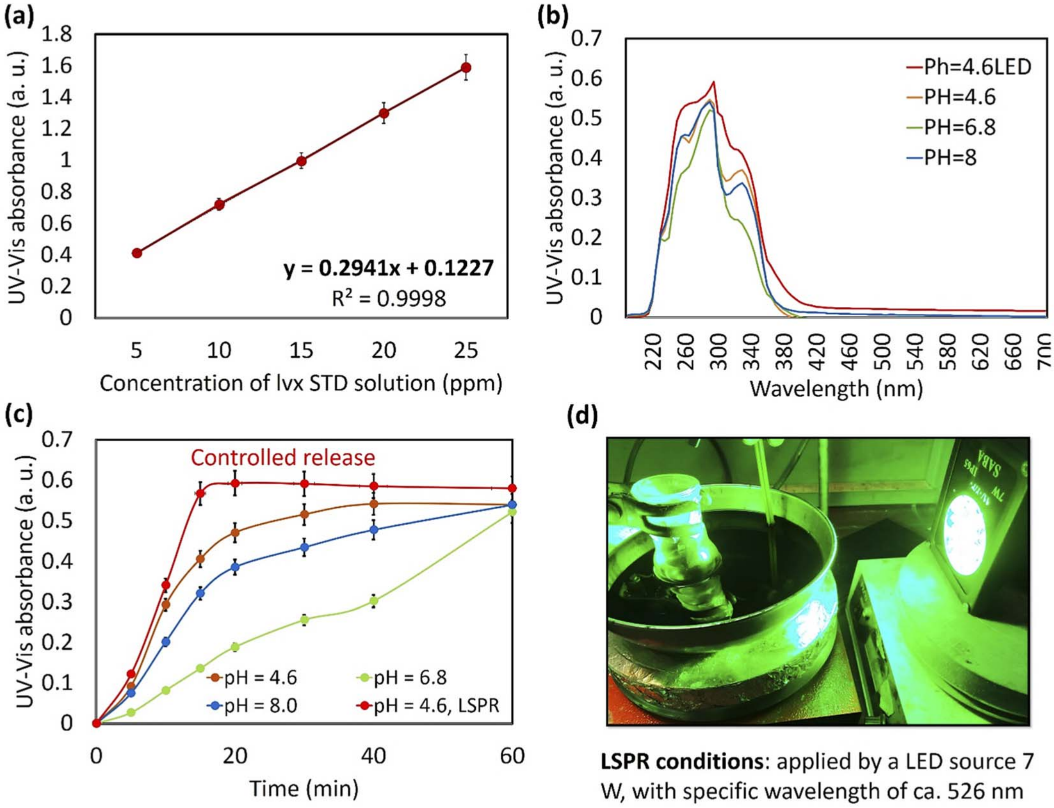

Fig. 7 (a) The calibration curve related to the STD solutions of lvx, (b) the UV-vis spectra related to the lvx@HNT/Au–CPP samples studied under different conditions after the drug release process, (c) the lvx-release profiles related to lvx@HNT/Au–CPP samples under different conditions [the error bars represent STDEV for the three repeated samples ($n = 3$)], and the (d) digital image of the LSPR conditions.

0.24) cm have been formed by the lvx@HNT/Au–CPP particles onto *S. aureus* and *E. coli* cells, respectively, whereas these values are reduced to (3.22 ± 0.08) cm and (3.88 ± 0.15) cm for the individual lvx with the same dosage (2.0 mg mL^{-1}) (Fig. 8c and f). This observation well confirms the high antimicrobial potency of the prepared lvx@HNT/Au–CPP nano-cargo, as only *ca.* 16 wt% of the administrated dose belongs to the lvx. In other words, a higher antimicrobial effect is obtained through the administration of the lvx@HNT/Au–CPP nano-cargo with less lvx content, in comparison with the individual lvx with the same dosage. The effect of the CPP sequence has also been investigated in the ZOI test. As is seen in Fig. 8b and e, two smaller zones with diameters of (2.66 ± 0.11) cm and (3.22 ± 0.12) cm were formed by lvx@HNT/Au (onto *S. aureus* and *E. coli* cells, respectively), at which the difference with the lvx@HNT/Au–CPP nano-cargo is only related to the absence of the CPP in the structure. On the other hand, Fig. 8c and f exhibit no inhibition zones for the individual CPP on both cell lines. This means that the conjugated CPP sequence participates in cell-penetration and solely includes no antibacterial effects. As another control, the photothermal cell killing potency of the AuNPs was monitored in the ZOI test. As shown in Fig. 8b and e, the zones with diameters of (1.82 ± 0.18) cm and (2.20 ± 0.14) cm were created by the individual AuNPs under irradiation of the green LED light. As previously discussed, these properties enhance the antimicrobial effects of the lvx@HNT/Au–CPP nano-cargo and provide a synergistic effect on bactericidal activities.

Table 3 The obtained results from drug release experiments on the lvx@HNT/Au–CPP nano-cargo

Entry	Conditions	Release time (min)	A[a] (A. U.)	Released lvx[b] (%)	Relative error[c] (%)
1	PBS, pH = 6.8, and 37 °C	60	0.522	84.8	1.2
2	PBS, pH = 8.0, and 37 °C	60	0.540	88.6	1.0
3	AcB, pH = 4.6, and 37 °C	40	0.542	89.0	1.2
4	AcB, pH = 4.6, and LED light	20	0.593	100.0	0.3

[a] The UV-vis absorbance value of the diluted samples (maximum value). [b] Calculations have been given in the ESI section. [c] Relative errors were calculated by considering STDEV for the three repeated samples ($n = 3$).

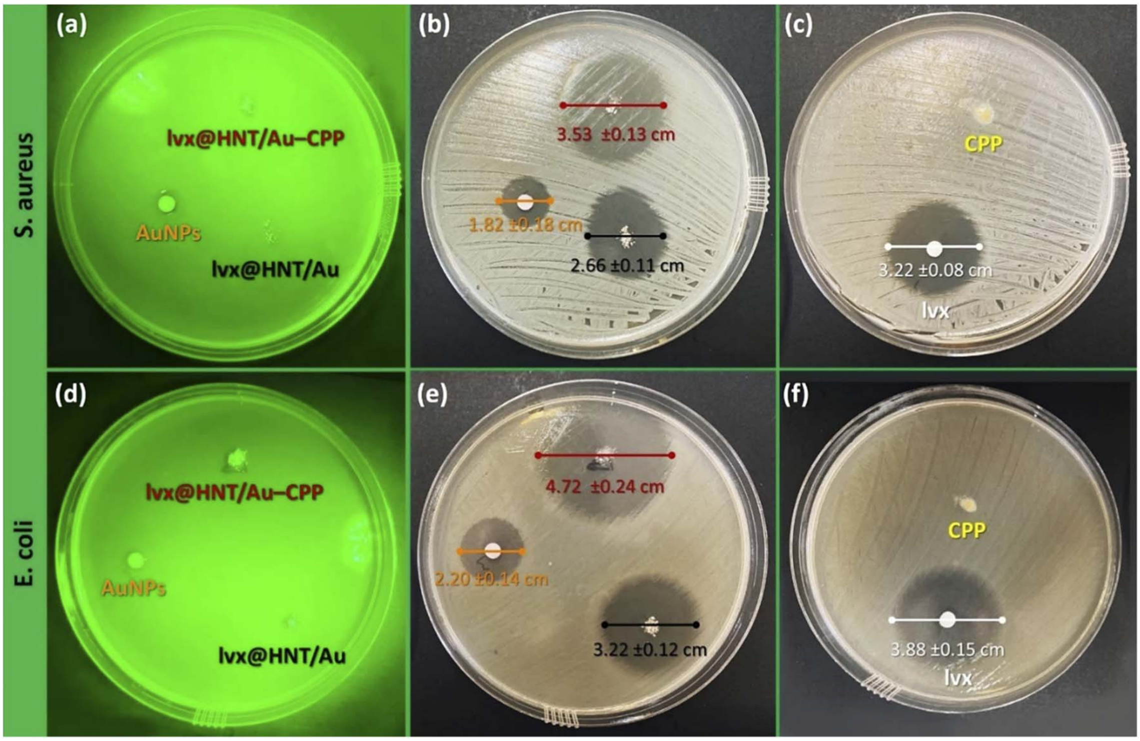

Fig. 8 Digital photos of the growth-inhibition zones created by the lvx@HNT/Au–CPP nano-cargo, lvx@HNT/Au, AuNPs, CPP sequence, and individual lvx (with an equal dosage: 2.0 mg) on *S. aureus* (a–c) and *E. coli* (d–f) cell lines [errors (±) represent absolute errors per three repeated samples ($n = 3$)].

The antimicrobial properties of the presented lvx@HNT/Au–CPP nano-cargo were further investigated *via* the colony counting method.[94] In this method, a linear pattern of the cell culture is executed on the agar gel. Then, a drop of the sample is poured around the disks. Afterward, the disks are put into the incubator (37 °C, 95% humidity) for 48 hours. The provided images of the disks are illustrated in Fig. 9. As is observed, the population of the disks containing lvx@HNT/Au–CPP (under LSPR conditions) decreased to zero, in comparison with both controls (*S. aureus* and *E. coli*), whereas there are 39 ± 12 and 36 ± 15 living cells of the *S. aureus* and *E. coli* strains, respectively, in the absence of the LED light (dark conditions). Also, it can be observed that all living cells (both strains) are dead with the same dosage of the individual lvx. Here again, it should be noted that the lvx content of the lvx@HNT/Au–CPP nano-cargo is only 16 wt%, and this is a great result to see a similar cell-killing activity by the lvx@HNT/Au–CPP nano-cargo, with the same concentration as the individual lvx. Also, the population of the disks was counted for the individual CPP and AuNPs as the controls. The related images of the disks have been given in the ESI section of this paper (Fig. S2).† As expected, no significant difference was observed between the populations of the controls and the CPP-contacting disks. In the case of the AuNPs, the population of the living cells (both strains) reduced to 424 ± 49 and 382 ± 33 (at darkness) and 369 ± 56 and 288 ± 29 (under LSPR conditions) for the *S. aureus* and *E. coli* strains, respectively.

3.3.3. Confocal microscopy. To study cell adhesion and killing potency of the prepared nano-cargo, confocal microscopy was performed on a dispersed sample of lvx@HNT/Au–CPP particles (in DMEM), subjected to the *S. aureus* and *E. coli* strains in the time range of 30–120 minutes.[95] In this way, cell staining was carried out using crystal violet ($\lambda_{\max} \sim 590$ nm) after each time of incubation.[96] Generally, cell adhesion and co-localization of the solid particles with the living cells can be discerned through merging two different colors that are chosen in the imaging process. In this study, the red color was dedicated to the lvx drug (loaded into the carriers), and the blue color was dedicated to the stained cells with crystal violet. As illustrated in Fig. 10, the lvx@HNT/Au–CPP particles (red spots) approached the cells (blue spots) during a 30 minute incubation. But, no vestige of the mixture of two colors (resulting in purple) is seen in the merge panel. This means that the lvx@HNT/Au–CPP particles are not attached to the living cells during this time. After 60 minutes, the particles have gotten closer to the cells and sporadically co-localized with them. Ultimately, it is clearly observed that the particles are more dispersed after 120 minutes and quite attached to the living cells. This result is confirmed by the intense purple color formed in the merge panel of 120 minutes. Moreover, it is observed that the volume of the *S. aureus* cells reduced after this time period, corroborating the high cell-killing potency of the prepared lvx@HNT/Au–CPP nano-cargo over a Gram-positive cell line. Actually, it is quite reasonable to observe higher

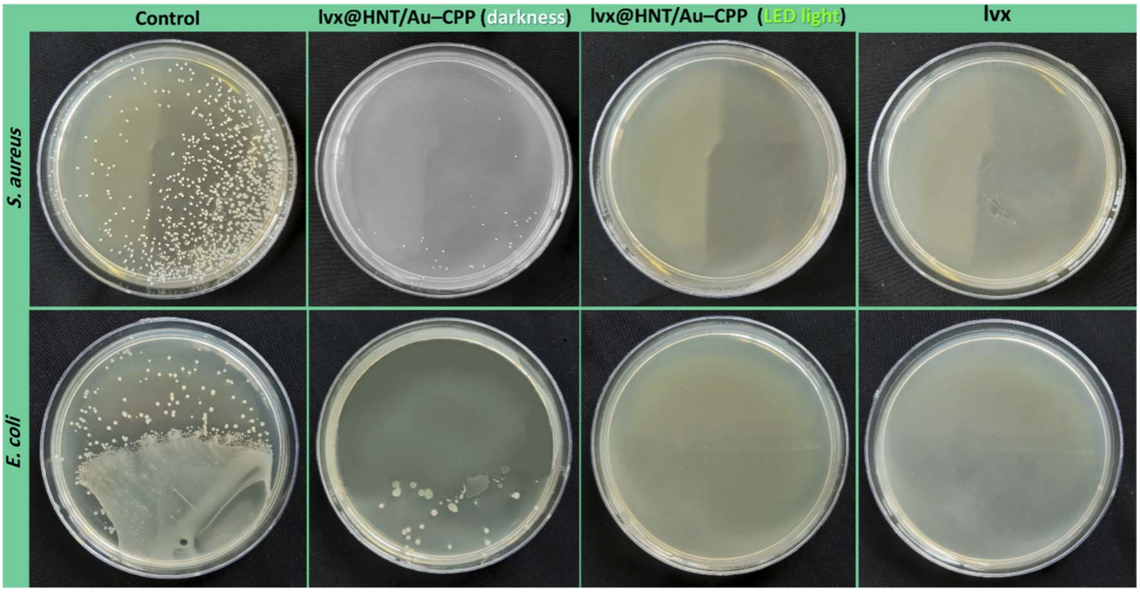

Fig. 9 Digital photos of colony count disks containing the lvx@HNT/Au–CPP nano-cargo under dark and LSPR conditions (LED light) and the individual lvx (with an equal dosage: 2.0 mg) on *S. aureus* and *E. coli* cell lines (incubated 48 hours at 37 °C and a humidity of 95%).

resistance by the *E. coli* cells (as a Gram-negative strain) because they contain a stronger cell membrane than the *S. aureus* cells.

3.3.4. Comparisons. So far, many similar drug delivery systems have been reported based on halloysite nanomaterials and antimicrobial peptide structures. Hence, it would be of high importance to highlight the advantages of the presented lvx@HNT/Au–CPP nano-cargo *via* true comparisons. Recently, a similar system has been reported by Khodabakhshi and Baghersad,[22] in which a guanidine-rich cell-penetrating peptide was considered for the conjugation onto halloysite surfaces. As the first and foremost challenge, it should be noted that the total yield of the peptide synthesis process is quite low because of steric hindrance by the structure of the arginine amino acid. Therefore, it can be stated that the finished cost for the preparation of a guanidine-rich sequence is higher than the CPP used in this work. In another report by Fakhrullina *et al.*, curcumin delivery to bacteria cells was carried out by a dextrin-coated halloysite system.[97] In this report, dextrin coated the halloysite nanotubes, but there is no responsive agent for swelling of the polymeric matrix and further release of curcumin. In the

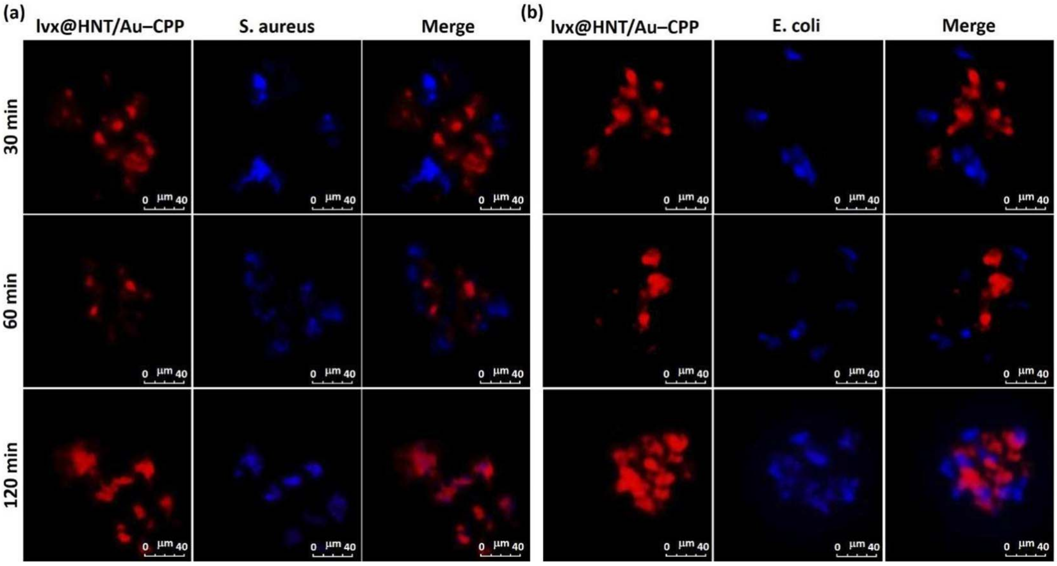

Fig. 10 Confocal microscopy images of the lvx@HNT/Au–CPP nano-cargo and stained cells: (a) *S. aureus* and (b) *E. coli*. The lvx@HNT/Au–CPP particles and the bacterial cells were incubated for 30, 60, and 120 minutes at 37 °C and a humidity of 95%. Cell staining has been carried out using crystal violet.

lvx@HNT/Au–CPP nano-cargo, AuNPs have been incorporated onto the surface of halloysite for plasmonic heating and LSPR-triggered release of levofloxacin. In 2017, Meria *et al.* introduced an active packaging material based on starch-halloysite nanocomposites incorporating antimicrobial peptides into the interior spaces and between the layers.[98] Generally, covalent conjugation of the peptide structures onto the surfaces is a more trustworthy pathway than the incorporation into the pores. In this case, deconjugation of the peptides (as a well-known structural instability) occurred less in comparison with the incorporated peptides in the tubes. This is why in this work, the surface of the halloysite nanotubes was initially modified by a silane compound. Based on the above comparisons, it can be concluded that the presented lvx@HNT/Au–CPP nano-cargo is an advanced version of previously reported antimicrobial halloysite nanomaterials.

4. Conclusion

In this report, the antimicrobial properties of lvx medication have been enhanced through the application of porous nanomaterials and drug delivery techniques. Concisely, a determined dosage of the lvx was incorporated into the HNTs, a clay-based nanostructure with high porosity. Then, the surface of the prepared lvx@HNT particles was decorated with the as-prepared AuNPs and conjugated to a cell-penetrating peptide (CPP), including glycine, alanine, phenylalanine, proline, histidine, and arginine amino acids. The architecture of the prepared nano-cargo (denoted as lvx@HNT/Au–CPP) has been precisely investigated by various analytical methods. The incorporated AuNPs played a vital role in the plasmonic release of the loaded lvx with high control. They also acted as a heating agent for the photothermal killing of the bacterial cells under irradiation of the green LED light (7 W). The obtained results have revealed a synergistic effect between the loaded lvx and photothermal cell-killing activity of the lvx@HNT/Au–CPP nano-cargo.

In summary, the measurements in the ZOI and colony-counting experiments have verified that a more potent antimicrobial activity is obtained by the designed lvx@HNT/Au–CPP nano-cargo, compared with the individual lvx with the exact dosage. Since the lvx content was estimated to be *ca.* 16 wt% of the total weight of lvx@HNT/Au–CPP, it is concluded that the therapeutic effect of the lvx has been significantly enhanced while a low dosage of the lvx is administered. As a result, it can be stated that the bacterial resistance to antibiotics and the toxic effects of the chemical medications are reduced by applying the presented strategy.

Conflicts of interest

The authors confirm that there is no conflict of interest.

Author contributions

Dr Reza Taheri-Ledari: ideation: supervision, peptide synthesis, writing, revision and editing, and graphics. Mr Mohammad Reza Ahghari: cellular experiments. Miss Fatemeh Ansari: all practical stages and analysis preparation. Miss Mohadeseh Forouzandeh-Malati: analysis preparation. Miss Seyedeh Shadi Mirmohammadi: practical stages. Mrs Simindokht Zarei-Shokat: practical stages. Dr Sorour Ramezanpour: pPeptide synthesis. Dr Wenjie Zhang: revision, editing, and financial support. Dr Ye Tian: supervision, ideation, revision and editing. Prof. Dr Ali Maleki: supervision and lead all stages of the work.

Acknowledgements

This work was partially supported by Sichuan Science and Technology Program (2022YFH0047). The authors appreciate partial support of Iran University of Science & Technology (IUST).

References

1 M. J. Ansari, S. A. Jasim, T. Z. Taban, D. O. Bokov, M. N. Shalaby, M. E. Al-Gazally, H. H. Kzar, M. T. Qasim, Y. F. Mustafa and M. Khatami, *J. Cluster Sci.*, 2022, 1–11.

2 W. Zhang, R. Taheri-Ledari, F. Ganjali, *et al.*, Nanoscale bioconjugates: A review of the structural attributes of drug-loaded nanocarrier conjugates for selective cancer therapy, *Heliyon*, 2022, **8**, e09577.

3 X. Zhang, Z. Chen, X. Liu, S. L Hanna, X. Wang, R. Taheri-Ledari, A. Maleki, P. Li and O. K Farha, *Chem. Soc. Rev.*, 2020, **49**, 7406–7427.

4 M. Amiri, P. Khazaeli, A. Salehabadi and M. Salavati-Niasari, *Adv. Colloid Interface Sci.*, 2021, **288**, 102316.

5 S. Parvaz, R. Taheri-Ledari, M. S. Esmaeili, M. Rabbani and A. Maleki, *Life Sci.*, 2020, **240**, 117099.

6 A. Maleki, R. Taheri-Ledari and M. Soroushnejad, *ChemistrySelect*, 2018, **3**, 13057–13062.

7 R. Taheri-Ledari, *Heterogeneous Micro and Nanoscale Composites for the Catalysis of Organic Reactions: Classification of micro and nanoscale Composites, Micro and Nano Technologies*, Elsevier, 2022, pp. 1–21.

8 R. Taheri-Ledari, W. Zhang, M. Radmanesh, S. S. Mirmohammadi, A. Maleki, N. Cathcart and V. Kitaev, *Small*, 2020, **16**, e2002733.

9 B. Cecen, A. Bal-Ozturk, G. Yasayan, E. Alarcin, P. Kocak, R. Tutar, L. D. Kozaci, S. R. Shin and A. K. Miri, *J. Biomed. Mater. Res., Part A*, 2022, **110**, 1147–1165.

10 F. Ganjali, A. Kashtiaray, S. Zarei-Shokat, R. Taheri-Ledari and A. Maleki, *Nanoscale Adv.*, 2022, **4**, 1263–1307.

11 R. Taheri-Ledari, F. Rasouli Asl, M. Saeidirad, A. Kashtiaray and A. Maleki, *Sci. Rep.*, 2022, **12**, 1–14.

12 A. Maleki, R. Taheri-Ledari, J. Rahimi, M. Soroushnejad and Z. Hajizadeh, *ACS Omega*, 2019, **4**, 10629–10639.

13 Z. Hajizadeh, K. Valadi, R. Taheri-Ledari and A. Maleki, *ChemistrySelect*, 2020, **5**, 2441–2448.

14 S. S. Soltani, R. Taheri-Ledari, S. M. F Farnia, A. Maleki and A. Foroumadi, *RSC Adv.*, 2020, **10**, 23359–23371.

15 R. Taheri-Ledari, M. Saeidirad, F. S. Qazi, A. Fazeli, A. Maleki and A. E. Shalan, *RSC Adv.*, 2021, **11**, 25284–25295.

16 F. Persano, S. Batasheva, G. Fakhrullina, G. Gigli, S. Leporatti and R. Fakhrullin, *J. Mater. Chem. B*, 2021, **9**, 2756–2784.

17 L. Lisuzzo, G. Cavallaro, S. Milioto and G. Lazzara, *Adv. Mater. Interfaces*, 2022, 2102346.

18 D. Peixoto, I. Pereira, M. Pereira-Silva, F. Veiga, M. R. Hamblin, Y. Lvov, M. Liu and A. C. Paiva-Santos, *Coord. Chem. Rev.*, 2021, **440**, 213956.

19 Y. Zhu, Y. Fu, A. Zhang, X. Wang, Z. Zhao, Y. Zhang, T. Yin, J. Gou, Y. Wang and H. He, *Eur. J. Pharm. Sci.*, 2022, **168**, 106047.

20 H. Mohtasham, B. Gholipour, S. Rostamnia, A. Ghiasi-Moaser, M. Farajzadeh, N. Nouruzi, H. W. Jang, R. S. Varma and M. Shokouhimehr, *Colloids Surf., A*, 2021, **614**, 126187.

21 R. Taheri-Ledari, W. Zhang, M. Radmanesh, N. Cathcart, A. Maleki and V. Kitaev, *J. Nanobiotechnol.*, 2021, **19**, 1–21.

22 M. R. Khodabakhshi and M. H. Baghersad, *RSC Adv.*, 2021, **11**, 38961–38976.

23 A. Karewicz, A. Machowska, M. Kasprzyk and G. Ledwójcik, *Materials*, 2021, **14**, 2943.

24 R. Taheri-Ledari, A. Fazeli, A. Kashtiaray, S. Salek Soltani, A. Maleki and W. Zhang, *Langmuir*, 2021, **38**, 132–146.

25 T. A. Tabish, P. Dey, S. Mosca, M. Salimi, F. Palombo, P. Matousek and N. Stone, *Adv. Sci.*, 2020, **7**, 1903441.

26 P. Gupta, S. Kar, A. Kumar, F.-G. Tseng, S. Pradhan, P. S. Mahapatra and T. S. Santra, *Analyst*, 2021, **146**, 4756–4766.

27 J. Ma, X. Wang, J. Feng, C. Huang and Z. Fan, *Small*, 2021, **17**, 2004287.

28 M. Mousavi, L. T. T. Moriyama, C. Grecco, M. S. Nogueira, K. Svanberg, C. Kurachi and S. Andersson Engels, *J. Biomed. Opt.*, 2020, **25**, 063812.

29 S. Chatterjee, X.-Y. Lou, F. Liang and Y.-W. Yang, *Coord. Chem. Rev.*, 2022, **459**, 214461.

30 R. Taheri-Ledari and A. Maleki, *New J. Chem.*, 2021, **45**, 4135–4146.

31 B. Andreiuk, F. Nicolson, L. M. Clark and S. R. Panikkanvalappil, *Nanotheranostics*, 2022, **6**, 10.

32 L. Wang, Z. Wang, L. Cao and K. Ge, *Biosaf. Health.*, 2022, **4**(3), 161–170.

33 M. Sharifi, F. Attar, A. A. Saboury, K. Akhtari, N. Hooshmand, A. Hasan, M. A. El-Sayed and M. Falahati, *J Control Release.*, 2019, **311**, 170–189.

34 M. Moros, A. Lewinska, F. Merola, P. Ferraro, M. Wnuk, A. Tino and C. Tortiglione, *ACS Appl. Mater. Interfaces*, 2020, **12**, 13718–13730.

35 V. P. Zharov, K. E. Mercer, E. N. Galitovskaya and M. S. Smeltzer, *Biophys. J.*, 2006, **90**, 619–627.

36 S. Yougbaré, H.-L. Chou, C.-H. Yang, D. I. Krisnawati, A. Jazidie, M. Nuh and T.-R. Kuo, *J. Hazard. Mater.*, 2021, **407**, 124617.

37 A. B. Engin and A. Engin, *Curr. Drug Metab.*, 2019, **20**, 720–741.

38 M. Á. Ortega, A. Guzmán Merino, O. Fraile-Martínez, J. Recio-Ruiz, L. Pekarek, L. G. Guijarro, N. García-Honduvilla, M. Álvarez-Mon, J. Buján and S. García-Gallego, *Pharmaceutics*, 2020, **12**, 874.

39 S. Satish, M. Tharmavaram and D. Rawtani, *Nanobiomedicine*, 2019, **6**, 1849543519863625.

40 Y. Lvov, W. Wang, L. Zhang and R. Fakhrullin, *Adv. Mater.*, 2016, **28**, 1227–1250.

41 V. Soltaninejad, M. R. Ahghari, R. Taheri-Ledari and A. Maleki, *Langmuir*, 2021, **37**, 4700–4713.

42 V. Van Giau, S. S. A. An and J. Hulme, *Drug Des., Dev. Ther.*, 2019, **13**, 327.

43 X. Zhao, Z. Yu and T. Ding, *Microorganisms*, 2020, **8**, 425.

44 N. H. Kamaruzaman, N. N. M. Noor, R. M. S. R. Mohamed, A. Al-Gheethi, S. K. Ponnusamy, A. Sharma and D.-V. N. Vo, *Environ. Res.*, 2022, **209**, 112831.

45 P. Sarkar, P. K. Issac, S. V. Raju, P. Elumalai, A. Arshad and J. Arockiaraj, *Aquacult. Res.*, 2021, **52**, 2361–2376.

46 H. Liu, N. Sun, P. Ding, C. Chen, Z. Wu, W. Zhu, L. Liu, Z. Wang and R. Pei, *Colloids Surf., B*, 2020, **191**, 110985.

47 P. Dramou, M. Fizir, A. Taleb, A. Itatahine, N. S. Dahiru, Y. A. Mehdi, L. Wei, J. Zhang and H. He, *Carbohydr. Polym.*, 2018, **197**, 117–127.

48 D. D. Hartwig, K. L. Bacelo, T. L. Oliveira, R. Schuch, F. K. Seixas, T. Collares, O. Rodrigues, C. P. Hartleben and O. A. Dellagostin, *Mem. Inst. Oswaldo Cruz*, 2015, **110**, 134–137.

49 S. Mojarad-Jabali, M. Farshbaf, P. R Walker, S. Hemmati, Y. Fatahi, P. Zakeri-Milani, M. Sarfraz and H. Valizadeh, *Int. J. Pharm.*, 2021, **602**, 120645.

50 Z. Zhao, A. Ukidve, V. Krishnan and S. Mitragotri, *Adv. Drug Delivery Rev.*, 2019, **143**, 3–21.

51 W. Zhang, R. Taheri-Ledari, Z. Hajizadeh, E. Zolfaghari, M. R. Ahghari, A. Maleki, M. R. Hamblin and Y. Tian, *Nanoscale*, 2020, **12**, 3855–3870.

52 R. Taheri-Ledari and A. Maleki, *J. Pept. Sci.*, 2020, **26**, e3277.

53 C. R. Hango, C. M. Backlund, H. C. Davis, N. D. Posey, L. M. Minter and G. N. Tew, *Biomacromolecules*, 2021, **22**, 2850–2863.

54 R. K. Deshmukh, K. Akhila, D. Ramakanth and K. K. Gaikwad, *Int. J. Biol. Macromol.*, 2022, **201**, 1–13.

55 C. R. Kaze, T. Alomayri, A. Hasan, S. Tome, G. L. Lecomte-Nana, J. G. D. Nemaleu, H. K. Tchakoute, E. Kamseu, U. C. Melo and h. Rahier, *Appl. Clay Sci.*, 2020, **196**, 105773.

56 L. E. Rodriguez, A. Bail, R. O. Castillo and G. G. Arízaga, *Curr. Pharm. Des.*, 2020, **26**, 650–663.

57 A. A. El-Soad, A. Pestov, D. Tambasova, V. Osipova, N. Martemyanov, G. Cavallaro, E. Kovaleva and G. Lazzara, *J. Organomet. Chem.*, 2020, **915**, 121224.

58 C. Arib, J. Spadavecchia and M. L. de la Chapelle, *Sci. Rep.*, 2021, **11**, 1–8.

59 N. Nouruzi, M. Dinari, B. Gholipour, N. Mokhtari, M. Farajzadeh, S. Rostamnia and M. Shokouhimehr, *Mol. Catal.*, 2022, **518**, 112058.

60 K. Bolaños, M. Sánchez-Navarro, E. Giralt, G. Acosta, F. Albericio, M. J. Kogan and E. Araya, *Mater. Sci. Eng., C*, 2021, **131**, 112512.

61 S. J. Raheem, B. W. Schmidt, V. R. Solomon, A. K. Salih and E. W. Price, *Bioconjugate Chem.*, 2020, **32**, 1204–1213.

62 Z. Ma, J. Liu, G. Shen, X. Zheng, Y. Pei and K. Tang, *Cellulose*, 2021, **28**, 6287–6303.

63 B. K. Korah, A. R. Chacko, T. Abraham and B. Mathew, *Part. Part. Syst. Charact.*, 2022, 2100264.

64 T. P. Popova, I. Ignatov, T. Petrova and G. Dinkov, *J. Pharm. Res. Int.*, 2021, **33**, 61–67.

65 I. Baghdadi, A. Zaazou, B. A. Tarboush, M. Zakhour, M. Özcan and Z. Salameh, *J. Mech. Behav. Biomed. Mater.*, 2020, **110**, 103892.

66 F. A. Hussain, J. Zamora, I. M. Ferrer, M. Kinyua and J. M. Velázquez, *Environ. Sci.: Water Res. Technol.*, 2020, **6**, 2035–2042.

67 J. Torres-Luna, S. Moreno, R. Molina and J. Carriazo, *Energy Fuels*, 2018, **32**, 9782–9792.

68 T. M. Dhameliya, H. A. Donga, P. V. Vaghela, B. G. Panchal, D. K. Sureja, K. B. Bodiwala and M. T. Chhabria, *RSC Adv.*, 2020, **10**, 32740–32820.

69 Q. He, J. Chen, J. Yan, S. Cai, H. Xiong and Y. Liu, *Asian J. Pharm. Sci.*, 2020, **15**, 416–448.

70 K. K. Hershberger, A. J. Gauger and L. M. Bronstein, *ACS Appl. Bio Mater.*, 2021, **4**, 4720–4736.

71 A. Maleki, R. Taheri-Ledari and R. Ghalavand, *Comb. Chem. High Throughput Screening*, 2020, **23**, 119–125.

72 R. Taheri-Ledari, A. Maleki, E. Zolfaghari, M. Radmanesh, H. Rabbani, A. Salimi and R. Fazel, *Ultrason. Sonochem.*, 2020, **61**, 104824.

73 I. Surya, K. Waesateh, A. Masa and N. Hayeemasae, *Polymers*, 2021, **13**, 3536.

74 S. Moghari, S. H. Jafari, M. K. Yazdi, M. Jouyandeh, A. Hejna, P. Zarrintaj and M. R. Saeb, *Nanomaterials*, 2021, **11**, 3078.

75 T. S. Gaaz, A. B. Sulong, A. A. H. Kadhum, M. H. Nassir and A. A. Al-Amiery, *Materials*, 2016, **9**, 620.

76 J. Hou, H. Ci, P. Wang, C. Wang, B. Lv, L. Miao and G. You, *J. Hazard. Mater.*, 2018, **360**, 319–328.

77 Q. Ong, T. Mao, N. I. Anaraki, Ł. Richter, C. Malinverni, X. Xu, F. Olgiati, P. H. J. Silva and A. Neels, *Mater. Horiz.*, 2022, **9**, 303–311.

78 C. I. Idumah, A. Hassan, J. Ogbu, J. Ndem and I. C. Nwuzor, *Compos. Interfaces*, 2019, **26**, 751–824.

79 M. J. Saif, H. M. Asif and M. Naveed, *J. Chil. Chem. Soc.*, 2018, **63**, 4109–4125.

80 M. He, T. Yang, Y. Wang, M. Wang, X. Chen, D. Ding, Y. Zheng and H. Chen, *Adv. Healthcare Mater.*, 2021, **10**, 2002104.

81 P. Zhang, P. Wang, L. Yan and L. Liu, *Int. J. Nanomed.*, 2018, **13**, 7047.

82 H. Su, X. Li, L. Huang, J. Cao, M. Zhang, V. Vedarethinam, W. Di, Z. Hu and K. Qian, *Adv. Mater.*, 2021, **33**, 2007978.

83 B. Zhang, L. Xu, Z. Zhao, S. Peng, C. Yu, X. Zhang, Y. Zong and D. Wu, *Sep. Purif. Technol.*, 2022, **285**, 120365.

84 S. A. Aromal and D. Philip, *Phys. E*, 2012, **44**, 1329–1334.

85 F. Hassanzadeh-Afruzi, F. Esmailzadeh, S. Asgharnasl, F. Ganjali, R. Taheri-Ledari and A. Maleki, *Sep. Purif. Technol.*, 2022, **291**, 120956.

86 P. Kumari, A. Kulkarni, A. K. Sharma and H. Chakrapani, *ACS omega*, 2018, **3**, 2155–2160.

87 H. Choi, A. Schulte, M. Müller, M. Park, S. Jo and H. Schönherr, *Adv. Healthcare Mater.*, 2021, **10**, 2100069.

88 S. D. Stojanović, J. M. Nićiforović, S. M. Živanović, J. V. Odović and R. M. Jelić, *Monatsh. Chem.*, 2020, **151**, 999–1007.

89 R. Yendluri, Y. Lvov, M. M. de Villiers, V. Vinokurov, E. Naumenko and R. Fakhrullin, *J. Pharm. Sci.*, 2017, **106**, 3131–3139.

90 S. Same, S. A. Nakhjavani, G. Samee and S. Davaran, *Ceram. Int.*, 2022, **48**(21), 31065–31079.

91 S. Shah, N. Shah, S. Amin, D. Mori, M. Soniwala and J. Chavda, *J. Pharm. Innov.*, 2022, 1–11.

92 T. Kaewchomphunuch, T. Charoenpichitnunt, V. Thongbaiyai, N. Ngamwongsatit and K. Kaeoket, *BMC Vet. Res.*, 2022, **18**, 1–13.

93 P. Singh, A. U. Mirza, A. H. Mondal, K. Mukhopadhyay and N. Nishat, *J. Appl. Polym. Sci.*, 2022, **139**, 51749.

94 S. Bala Subramaniyan, S. Ramesh, S. Rajendran and A. Veerappan, *Bioconjugate Chem.*, 2021, **32**, 1823–1833.

95 Z. Qin, Y. Zheng, T. Du, Y. Wang, H. Gao, J. Quan, Y. Zhang, Y. Du, L. Yin and X. Wang, *Chem. Eng. J.*, 2021, **414**, 128779.

96 A. Valliammai, S. Sethupathy, A. Priya, A. Selvaraj, J. P. Bhaskar, V. Krishnan and S. K. Pandian, *Sci. Rep.*, 2019, **9**, 1–16.

97 G. Fakhrullina, E. Khakimova, F. Akhatova, G. Lazzara, F. Parisi and R. Fakhrullin, *ACS Appl. Mater. Interfaces*, 2019, **11**, 23050–23064.

98 S. M. M. Meira, G. Zehetmeyer, J. O. Werner and A. Brandelli, *Food Hydrocolloids*, 2017, **63**, 561–570.